The influence of branched alkyl side chains in A-D-A oligothiophenes on the photovoltaic performance and morphology of solution-processed bulk-heterojunction solar cells

Ibrahim Ata, Sadok Ben Dkhil, Martin Pfannmoeller, Sara Bals, David Duche, Jean-Jacques Simon, Tomoyuki Koganezawa, Noriyuki Yoshimoto, Christine Videlot-Ackermann, Olivier Margeat, et al.

The influence of branched alkyl side chains in A-D-A oligothiophenes on the photovoltaic performance and morphology of solution-processed bulk-heterojunction solar cells

ORGANIC CHEMISTRY
FRONTIERS

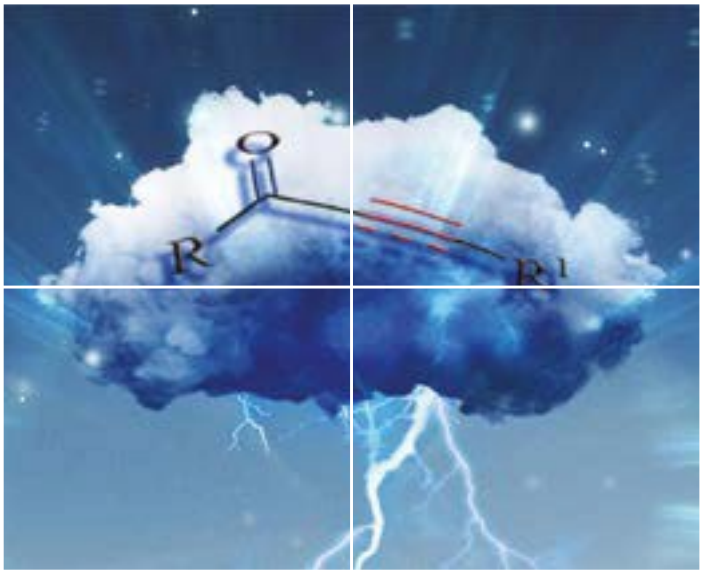

Accepted Manuscript

This article can be cited before page numbers have been issued, to do this please use: P. Baeuerle, I. Ata, S. B. Dkhil, M. Pfannmöller, S. Bals, D. Duché, J. Simon, C. Videlot-Ackermann, O. Margeat, J. Ackermann, N. Yoshimoto and T. Koganezawa, *Org. Chem. Front.*, 2017, DOI: 10.1039/C7QO00222J.

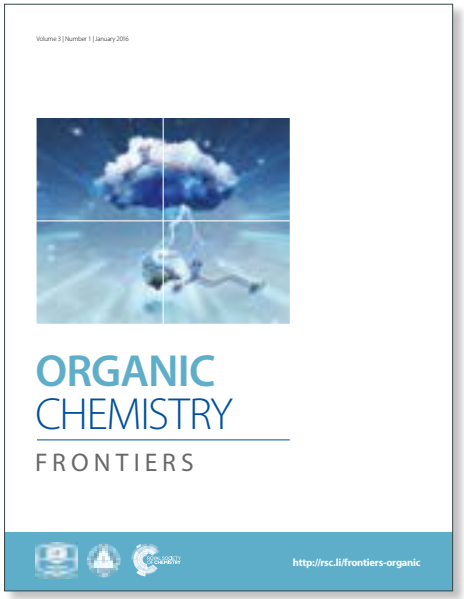

This is an Accepted Manuscript, which has been through the Royal Society of Chemistry peer review process and has been accepted for publication.

Accepted Manuscripts are published online shortly after acceptance, before technical editing, formatting and proof reading. Using this free service, authors can make their results available to the community, in citable form, before we publish the edited article. We will replace this Accepted Manuscript with the edited and formatted Advance Article as soon as it is available.

You can find more information about Accepted Manuscripts in the author guidelines.

Please note that technical editing may introduce minor changes to the text and/or graphics, which may alter content. The journal's standard Terms & Conditions and the ethical guidelines, outlined in our author and reviewer resource centre, still apply. In no event shall the Royal Society of Chemistry be held responsible for any errors or omissions in this Accepted Manuscript or any consequences arising from the use of any information it contains.

View Article Online
DOI: 10.1039/C7QO00222J

Full Paper for Org. Chem. Front.

The Influence of Branched Alkyl Side Chains in A-D-A Oligothiophenes on the Photovoltaic Performance and Morphology of Solution-processed Bulk-heterojunction Solar Cells

Ibrahim Ata,[a] Sadok Ben Dkhil,[b] Martin Pfannmöller,[c] Sara Bals,[d] David Duché,[e] Jean-Jacques Simon,[e] Tomoyuki Koganezawa,[f] Noriyuki Yoshimoto,[g] Christine Videlot-Ackermann,[b] Olivier Margeat,[b] Jörg Ackermann,[b] Peter Bäuerle[a]**

a: Dr. I. Ata, Prof. P. Bäuerle
Institute of Organic Chemistry II and Advanced Materials,
University of Ulm, Albert-Einstein-Allee 11
89081 Ulm, Germany
E-mail: peter.baeuerle@uni-ulm.de

b: Dr. J. Ackermann, S. Ben Dkhil, Christine Videlot-Ackermann, Olivier Margeat,
Centre Interdisciplinaire de Nanoscience de Marseille
CINAM UMR CNRS 7325
Campus de Luminy
13288 Marseille Cedex 09, France

c: Dr. M. Pfannmöller,
Centre for Advanced Materials
Heidelberg University
Im Neuenheimer Feld 225
69120 Heidelberg, Germany

d: Prof. Sara Bals
Electron Microscopy for Materials Research (EMAT)
University of Antwerp
Groenenborgerlaan 171
2020 Antwerpen, Belgium

e: Dr. David Duché, Prof. Jean-Jacques Simon Aix Marseille Université, CNRS, Université de Toulon IM2NP UMR 7334, 13397, Marseille, France

f: Dr. Tomoyuki Koganezawa
Industrial Application Division, Japan Synchrotron Radiation Research Institute, 1-1-1 Kouto, Sayo, Hyogo 679-5198, Japan.

g: Prof. Noriyuki Yoshimoto
Faculty of Science and Engineering, Iwate University, 4-3-5 Ueda, Morioka 020-8551, Japan.

Keywords: alkyl chain modification, morphology, oligothiophene, bulk-heterojunction solar cells, solvent vapor annealing, transmission electron microscopy

View Article Online
DOI: 10.1039/C7QO00222J

Abstract

Besides providing sufficient solubility, branched alky chains also affect the film-forming and packing properties of organic semiconductors. In order to avoid steric hindrance as it is present in wide-spread alkyl chains comprising the branching point position at the C2-position, i.e., 2-ethylhexyl, the branching point can be moved away from the π-conjugated backbone. In this report, we study the influence of the modification of the branching point position from the C2-position in 2-hexyldecylamine (**1**) to the C4-position in 4-hexyldecylamine (**2**) connected to the central diethieno[3,2-*b*:2',3'-*d*]pyrrole (DTP) moiety in a well-studied A-D-A oligothiophene onto the optoelectronic properties and photovoltaic performance in solution-processed bulk heterojunction solar cells (BHJSC) with [6,6]-phenyl-C71-butyric acid methyl ester ($PC_{71}BM$) as acceptor material. Post-treatment of the photoactive layers is performed *via* solvent vapor annealing (SVA) in order to improve the film microstructure of the bulk heterojunction. The time evolution of nanoscale morphological changes is accompanied by combining scanning transmission electron microscopy with low-energy-loss spectroscopy (STEM-SI), solid-state absorption spectroscopy, and two-dimensional grazing incidence X-ray diffraction (2D-GIXRD). Our results show an improvement of the photovoltaic performance dependent on the branching point position in the donor oligomer. Optical spacers are utilized to increase light absorption inside the co-oligomer **2**-based BHJSCs leading to increased power conversion efficiencies (PCE) of 8.2% when compared to corresponding co-oligomer **1**-based devices. STEM-SI analysis of respective device cross-sections of active layers containing **1** and **2** as donor materials indeed reveal significant differences in their respective active layer morphology.

1. Introduction

In recent years, bulk-heterojunction solar cells (BHJSC) consisting of a photoactive layer, in which the donor and acceptor components form interdigitating networks, have proven them-

View Article Online
DOI: 10.1039/C7QO00222J

selves as a promising device structure for high-performance solar cells.[1] Lately, huge advances were accomplished in terms of developing oligomeric donor materials, often referred to as small molecules, with tailored optoelectronic properties as well as alternative device architectures and optimization methods resulting in efficiencies (PCE) above 11% in single-junction devices.[2–4] The key to such highly efficient solar cells also lies in the control of the active layer morphology, more precisely, in the spatial distribution and the domain size of donor- and acceptor-rich phases. The blend-layer morphology is a delicate equilibrium, which can be adjusted by the use of additives, thermal annealing, or solvent vapor annealing (SVA). The latter post-treatment method, in which the casted blend layers are exposed to solvent vapor for an exact period of time was found to be the most effective alternative for highly-soluble A-D-A-type oligothiophenes, as previously reported.[5–8]

The design of photoactive materials typically focuses on the development of novel π-conjugated backbones or the modification thereof. In contrast, less effort was invested in the development of flexible side chains since they were merely introduced as solubilizing groups to enable purification and to facilitate satisfactory processing conditions. Generally, alkyl side chains are regarded as insulating parts of the material with negligible influence on optoelectronic properties of π-conjugated systems. Their significant impact on molecular packing, thin film morphology, and hence device performance is sometimes underestimated and the obtained results for materials with different alkyl side chains were particularly related to different solubility. Besides providing sufficient solubility, branched alkyl chains attached to the π-conjugated backbone also affect packing properties of organic semiconductors. Interestingly, the most-commonly used branched alkyl chains have their branching point at the C2-position, e.g., 2-ethylhexyl or 2-hexyldecyl, most probably owed to a good availability of corresponding building blocks and reagents.[9] However, a branching point at the C2-position may cause a steric repulsion between the π-system and the alkyl side chain.[9]

View Article Online
DOI: 10.1039/C7QO00222J

The group of Park investigated the effect of side chain characteristics on the photovoltaic performance for co-oligomers decorated with branched 2-ethylhexyl in comparison to linear octyl side chains at the central benzodithiophene (BDT) moieties.[10] Optoelectronic characterization pointed to slightly higher absorption, a smaller band gap, and a more planar structure for the oligomer comprising the branched side chains. This rather unexpected result was also reflected in a superior hole mobility and photovoltaic properties compared to the octyl-substituted co-oligomer (2.4% vs 1.3% efficiency). This effect was ascribed to the tighter packing of the 2-ethylhexyl-substituted co-oligomer as evidenced from XRD analysis.

In this respect, the group of Pei investigated how the positon of the branching point in alkyl side chains influenced the charge carrier transport properties of isoindigo-based polymers.[11] Although it may seem that polymeric field effect transistors are off the topic of oligomer-based BHJSCs, the obtained relationship between side-chain modification and mobility in thin films should be as well applicable to π-conjugated oligomeric donor materials and may help to deduce important design rules. It turned out that polymers with an alkyl chain branching point at the C4-carbon atom gave the highest hole mobilities manifesting itself as an empirical optimum. This relationship was also observed by other researches and obviously constitutes a recurring phenomenon.[12]

Inspired by these studies, the strategy to structurally optimize highly efficient A-D-A oligothiophene **1**, which comprises a 2-hexyldecyl chain at the central nitrogen of the dithienopyrrole (DTP) unit (Figure 1, top) and gives excellent results in solution-processed bulk-heterojunction solar cells (BHJSC),[5–7] was the movement of the branching point of the 2-hexyldecyl chain in **1** to the C4-position resulting in a 4-hexyldecyl side chain in **2** (Figure 1, bottom). By this relatively subtle structural modification realized in derivative **2**, which represents an isomer of **1**, the optoelectronic properties should remain rather unchanged, whereas the molecular packing and the morphology of the photoactive layer in the BHJ might be influ-

View Article Online
DOI: 10.1039/C7QO00222J

enced. The established and optimized device fabrication protocol for **1** should remain applicable for **2** due to the very similar molecular structure.

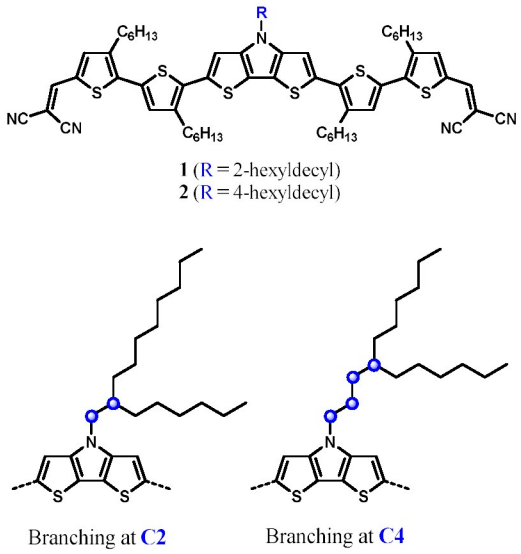

Figure 1: Chemical structures of isomeric A-D-A oligothiophenes **1** and **2** (top); Central DTP units substituted with hexyldecyl side chains branched at the C2- (left) and the C4-position (right), respectively.

We therefore elaborated a multi-step synthesis of branched 4-hexyldecan-1-amine **11**, which represents the central reagent for the synthesis of DTP-building block **13** used for the final assembly of oligothiophene **2**. Besides optoelectronic properties of the two isomeric co-oligomers **1** and **2**, we describe the fabrication of solution-processed BHJSCs and their optimization via implementation of optical spacer layers (ZnO) and treatment with SVA leading to device efficiencies over 8%. Finally, by combining scanning transmission electron microscopy and low-energy-loss spectroscopy we find clear evidence how the subtle change of the branching position in the side chain influences the morphology and phase separation of the photoactive layer which can be correlated to the device performance.

2. Synthesis

The synthesis route for DTP-oligothiophene **2** was designed according to the previously reported synthesis of isomeric analogue **1** and other DCV-endcapped oligothiophenes.[14] Thus,

View Article Online
DOI: 10.1039/C7QO00222J

for the preparation of the central *N*-(4-hexyldecyl)-dithieno[3,2-*b*:2',3'-*d*]pyrrole unit, 3,3'-dibromo-2,2'-bithiophene **12**, which is obtained according to a literature procedure,[15] should be reacted with 4-hexyldecan-1-amine **11** via Pd-catalyzed double Buchwald-Hartwig amination. Amine **11** is neither commercially available nor reported in literature. The synthesis of primary amines comprising longer alkyl chains branched at C4, for example 4-decyltetradecan-1-amine, was described in a patent, which was used as a guideline for our synthesis of 4-hexyldecan-1-amine **11.**[16] The synthesis of precursor **5** was performed according to the patent, whereas the subsequent synthetic steps were not always applicable for the synthesis of amine **11** and were changed or optimized. Therefore, we here describe this synthesis in detail and the final elaborated synthetic route is depicted in Scheme 1.

As the first step, commercially available 1,4-butanediole **3** was protected at one hydroxyl moiety by a benzyl group to yield **4** in 93% yield.[16] The next step was the Jones-oxidation of the free hydroxyl group to a carboxylic acid and subsequent esterification to give intermediate **5** in 83% yield. Ester **5** was reacted with the Grignard reagent of 1-bromohexane to tertiary alcohol **6**, which was isolated as a colorless liquid in 57% yield. The formal elimination of water from **6** was performed using Et_3SiH and an excess of trifluoro acetic acid (TFA) and 52% of olefin **7** were obtained. The subsequent catalytic hydrogenation of the olefinic double bond in **7** to alcohol **8** was achieved in 95% yield by introducing hydrogen gas in a continuous flow through the reaction mixture. The resulting branched alcohol **8** was iodinated under Appel conditions with PPh_3 as ligand and imidazole as base resulting in 4-hexyl-1-iododecan **9** in 97% yield. In a nucleophilic substitution reaction of iodide **9** with sodium azide in DMF, the corresponding azide **10** was obtained in 89% yield which was further converted to target 4-hexyldecan-1-amine **11** in 86% yield by reduction with $LiAlH_4$.

In the next step to DTP-oligothiophene **2**, 3,3'-dibromo-2,2'-bithiophene **12** was reacted with amine **11** in a Pd-catalyzed Buchwald-Hartwig amination to give 4-hexyldecyl-substituted DTP **13** in 94% yield. Full conversion of DTP **13** to distannyl **14** was achieved with 2.2

View Article Online
DOI: 10.1039/C7QO00222J

equivalents of *n*-BuLi and subsequent quenching with trimethylstannyl chloride as reported in literature.[14] In a final Stille-type cross-coupling step, distannylated DTP **14** was reacted with literature-known dicyanovinylene-substituted dihexyl-bithiophene **15** and $Pd(PPh_3)_4$ as catalyst in DMF to target oligomer **2** in 83% yield which was obtained as a dark purple solid (Scheme 2).[17] The structure and purity of **2** was proven via ^{1}H-NMR and ^{13}C-NMR spectroscopy and high resolution mass spectrometry.

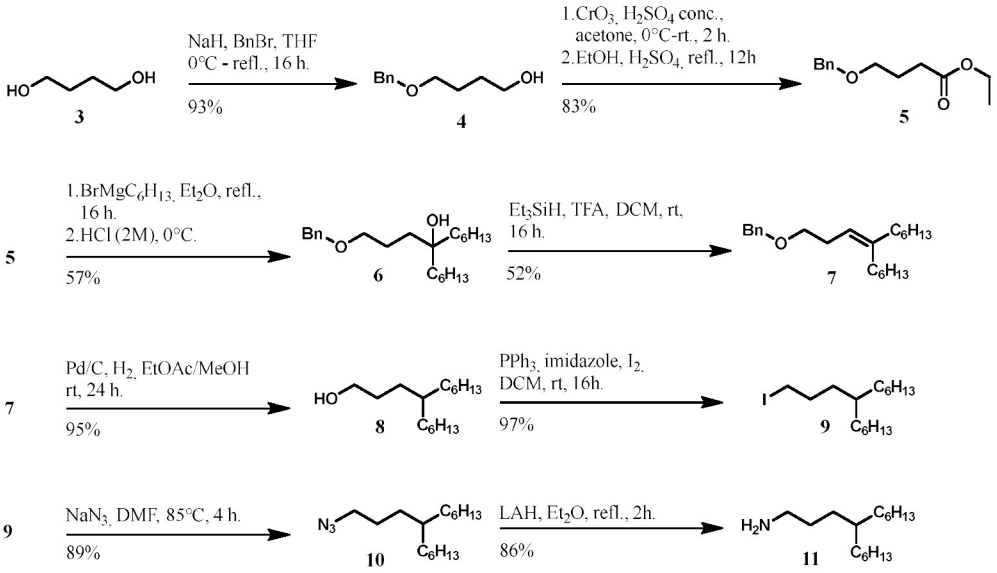

Scheme 1: Synthetic pathway for the preparation of 4-hexyldecan-1-amine **11**.

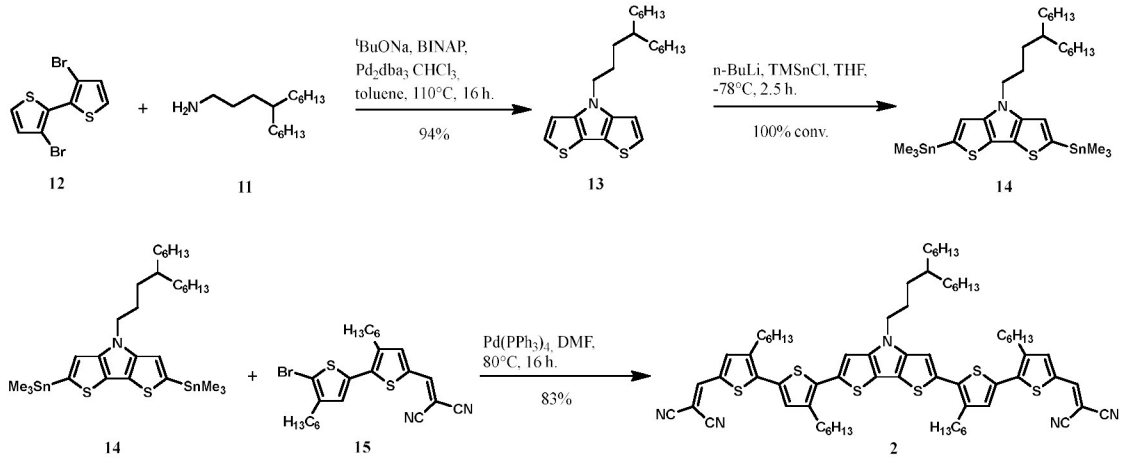

Scheme 2: Synthetic pathway for the preparation of DTP-oligothiophene **2**.

View Article Online
DOI: 10.1039/C7QO00222J

3. Optical and electrochemical properties

The optical properties of oligomer **2** were investigated by UV-vis spectroscopy in dichloromethane (DCM) solution and were compared to those of **1**. The optical data is summarized in Table 1. The absorption spectrum of **2** exhibited two main absorption bands with maxima at 399 nm and 563 nm, respectively, along with a good spectral coverage between 350-650 nm as depicted in Figure 2a. The high energy absorption band is assigned to π-π* transitions of the oligothiophene backbone, whereas the low energy transition band displays a high degree of internal charge transfer (ICT) character. Thin films for solid-state absorption spectra of oligomer **2** were prepared by spin-coating a corresponding solution (c = 4 mg mL^{-1} in chloroform) on glass substrates and the UV-vis spectrum is as well depicted in Figure 2a. The absorption bands and the onset of **2** were red-shifted by approximately 100 nm compared to the solution spectrum leading to a decreased optical gap of 1.6 eV in the neat film (Table 1). This typical effect we address to increased planarization and π-π stacking of the oligomers upon solidification.

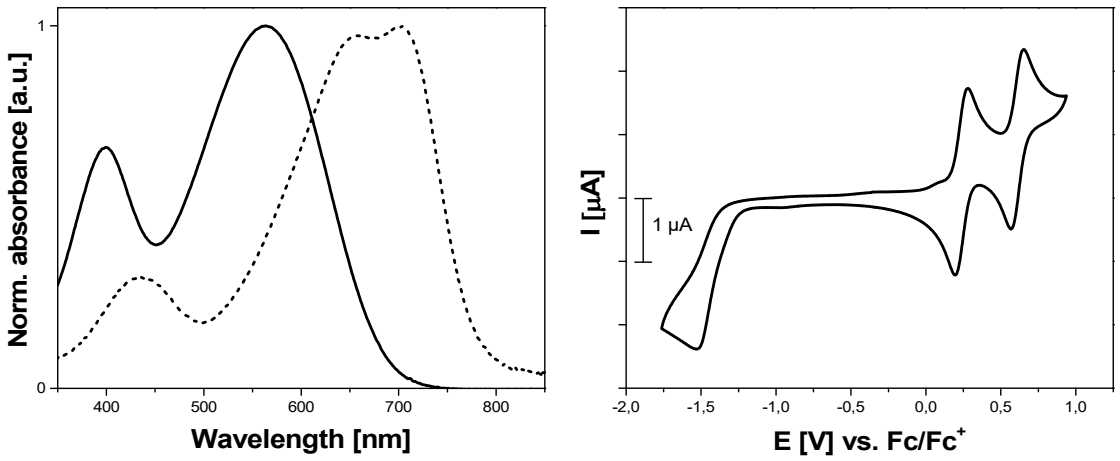

Figure 2: a) Absorption spectrum of oligomer **2** in DCM solution (bold line) and as thin film on a glass substrate (dotted line). **b)** Cyclic voltammogram of **2** measured in DCM using (n-Bu)$_4$NPF$_6$ (0.1 M) as supporting electrolyte at 100 mV s^{-1}, c = 10^{-3} M at room temperature.

The redox properties of oligothiophenes **2** were determined by cyclic voltammetry in DCM and tetrabutylammonium hexafluorophosphate ((n-Bu)$_4$NPF$_6$) as supporting electrolyte and

View Article Online
DOI: 10.1039/C7QO00222J

were compared to those of **1** (Figure 2b). Redox potentials, the electrochemical gaps, as well as HOMO (highest occupied molecular orbital) and LUMO (lowest unoccupied molecular orbital) energy levels are summarized in Table 1. Two reversible one-electron oxidation ($2x1e^-$) processes ($E_{ox1} \approx 0.25$ V; $E_{ox2} \approx 0.61$ V) were observed for the two oligomers **1** and **2** at nearly the same potentials, which are assigned to the formation of stable radical cations and dications, respectively, located on the central oligothiophene block. In the negative potential regime, an irreversible reduction wave for the simultaneous reduction of the DCV-acceptor units ($E_{red1} \approx -1.42$ V) has been observed. The HOMO (≈ -5.28 eV) and LUMO energy levels (≈ -3.70 eV) of the two oligomers were calculated from the onset of the first oxidation and reduction wave. The resulting electrochemical gaps were around 1.58 eV. The very small variation of the absorption and redox potential data for the two isomeric oligomers **1** and **2** well reflects that as expected the different side chains and branching position at the DTP-unit only marginally influences the electronic properties of the conjugated backbone in solution and in thin films.

Table 1. Optical and electrochemical data of oligomer **2** compared to **1**[5].

Oligomer	λ_{abs}^{sol} [nm][a]	ε [M^{-1} cm^{-1}]	E_g^{opt} sol [eV][a]	λ_{abs} film [nm][b]	E_g^{opt} film [eV][b]	E_{ox1} [V][c]	E_{ox2} [V][c]	E_{red1} [V][c]	HOMO [eV][d]	LUMO [eV][d]	E_g^{CV} [eV][e]
2	563, 399	61200	1.8	702, 658[f]	1.6	0.25	0.61	-1.42	-5.28	-3.70	1.58
1	560, 400	58400	1.8	700, 643[f]	1.6	0.27	0.63	-1.47	-5.30	-3.73	1.57

[a] Absorption measured in DCM solution (c = 10^{-6} M), λ_{max} is underlined. [b] Film spin-coated from $CHCl_3$ solution. [c] CV measured in DCM (n-Bu)$_4$NPF$_6$ (0.1M) as supporting electrolyte, potentials vs. Fc/Fc$^+$ at 100 mV s^{-1}. [d] E_{HOMO} and E_{LUMO} calculated from the onset of E_{ox1} and E_{red1}, respectively; relative to the Fc/Fc$^+$-couple with a calculated absolute energy of -5.1 eV vs vacuum. [e] Band gap calculated with $\Delta E_{CV} = E_{HOMO} - E_{LUMO}$. [f] Shoulder.

4. Photovoltaic performance

In order to evaluate the photovoltaic properties of oligomer **2** compared to the former donor **1**, we solution-processed BHJSCs using a regular device structure consisting of a glass/ITO/PEDOT:PSS/oligomer **2**:$PC_{71}BM$/ZnO/Al stack as shown in Figure 3. Importantly, the device structure as well as the SVA setup were identical to our recent study using **1** as do-

View Article Online
DOI: 10.1039/C7QO00222J

nor.[8] The first general observation during blend solution preparation is the difference in solubility of both isomers. Oligothiophene **2** exhibited a very high solubility in chloroform (84 mg/ml), which is by far sufficient in order to obtain good film-forming properties. Interestingly, isomeric oligomer **1** showed an even higher solubility of 123 mg/mL. Therefore, oligomer **2** (84 mg/mL in $CHCl_3$) needed longer stirring time to fully dissolve compared to oligomer **1** while preparing the blend solutions. To process the devices, we spin-coated blends of donor **2** and [6,6]-phenyl-C71-butyric acid methyl ester ($PC_{71}BM$) as electron acceptor from chloroform onto PEDOT:PSS- covered ITO substrates followed by the SVA treatment. The devices were completed by first depositing ZnO layers from isopropanol solution on top of the SVA-treated blend followed by deposition of the Al cathode by thermal evaporation (Figure 3). Thereby, the devices were optimized with regards to standard parameters such as D/A-ratio, donor concentration by keeping D/A-ratio constant, layer thickness, SVA time, and the implementation of an optical spacer layer consisting of ZnO-nanoparticles. The current density-voltage (J-V) characteristics, external (EQE), and internal quantum efficiency (IQE) spectra as well as thin film absorption spectra of the BHJSC devices for **2** / $PC_{71}BM$ are shown in Figure 4 and summarized in Table 2.

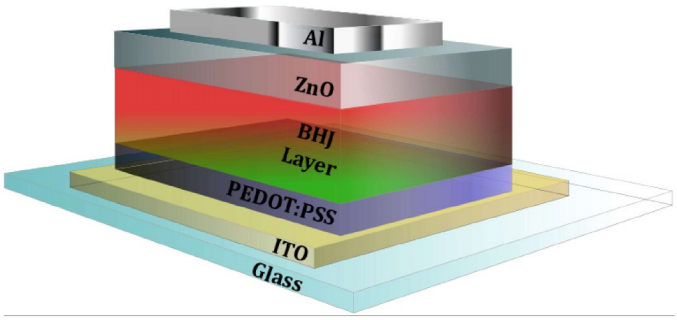

Figure 3: Schematic architecture of BHJSCs comprising oligomer **2** / $PC_{71}BM$ as photoactive layer and a ZnO-optical spacer layer.

View Article Online
DOI: 10.1039/C7QO00222J

First optimization experiments showed a clear trend that blend solutions with a D/A-ratio of 1:2 afforded the best results in terms of J_{SC} and PCE. Furthermore, we observed that a donor concentration of 8 mg/ml led to better device performance and to an active-layer thickness of approximately 95 nm which was determined as optimal, since the best photovoltaic parameters for untreated and post-treated devices were obtained for this layer thickness. The optimization of the optical spacer layer consisting of ZnO resulted in an optimal layer thickness of 30 nm. As-cast devices gave a rather low performance with J_{SC} of 3.44 mA cm^{-2} combined with V_{OC} of 0.78 V and FF of 29 % resulting in a device efficiency of 0.77%. In accordance to our recent work,[8] the PCE was drastically increased to 5.66%, when the photoactive layer was post-treated with chloroform vapor (SVA) for only 10 s after coating. SVA mainly influenced the photocurrent density and the fill factor. An increase of the SVA time to 30 s gave an excellent device performance with a PCE of 8.16%, a J_{SC} of 13.62 mA cm^{-2}, a V_{OC} of 0.79 V, and FF of 75% (Figure 4a). These conditions were obviously close to optimum since longer SVA times (60 s) resulted in deterioration of the photovoltaic parameters (Table 2). Comparing optimized photovoltaic data obtained for the novel (4-hexyldecyl)-DTP oligothiophene **2** with data of isomeric **1** (2-hexyldecyl) prepared under identical SVA conditions of 30 s, also yielded the best performance of J_{SC} = 12.74 mA cm^{-2}, V_{OC} = 0.84 V, and FF = 72% leading to a PCE of 7.74%.[8] It is worth to emphasize that compared to solar cells with oligomer **1** the photocurrent was increased by about 1 mA/cm^2. Furthermore, the increase of the fill factor to 75% obtained for a device of an active area of 0.2 cm^2 indicates highly efficient charge carrier extraction and low recombination inside devices based on oligomer **2**. However, comparing the V_{OC} in optimized devices, we see that after optimization devices based on **2** showed a clear loss of around 40 mV compared to **1**, although the energy level of both molecules are identical. The difference may be related to the nanoscale morphology of the photoactive layer, which will be discussed later.

View Article Online
DOI: 10.1039/C7QO00222J

Table 2: Photovoltaic parameters of BHJSCs containing oligomer **2** as donor and $PC_{71}BM$ as acceptor in a blend ratio of 1:2 in dependence of the solvent vapor annealing (SVA) time (chloroform). The data is compared to this of oligomer **1**, which was investigated using identical device setups and interfacial layers as published recently.[8]

Oligomer	SVA [s]	J_{SC} [mA cm^{-2}]	V_{OC} [V]	FF [%]	PCE_{max} [%]
2	0	3.44	0.78	29	0.77
2	10	12.59	0.80	57	5.66
2	30	13.62	0.79	75	8.16
2	60	10.52	0.81	71	6.06
1	30	12.74	0.84	72	7.74

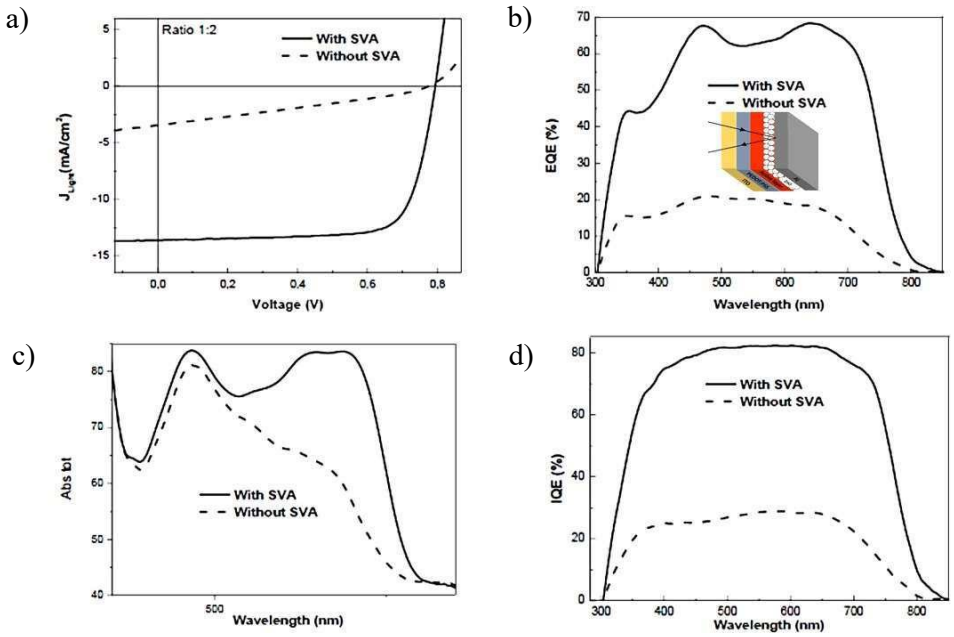

Figure 4: a) *J-V*-curves, **b)** EQE spectra, **c)** solid-state absorption spectra, and **d)** IQE spectra of BHJ-SCs containing oligomer **2 as** donor and $PC_{71}BM$ as acceptor (1:2) before and after 30 s of SVA with chloroform.

The effect of SVA is as well very clearly seen in the EQE and IQE spectra before and after the treatment: Over the whole absorption regime (300-850 nm) the quantum efficiencies are improved by a factor of 3-4 reaching 68% EQE @ 642 nm and 82% IQE @ 500-700 nm, respectively (Figure 4b, 4d). The vast enhancement in solar cell performance after 30 seconds of SVA suggests changes in the active layer morphology. The thin film absorption of the as-cast active layer displayed a prominent absorption band in the high energy region due to $PC_{71}BM$, whereas the oligomer absorption at wavelengths above 500 nm showed significantly lower in-

View Article Online
DOI: 10.1039/C7QO00222J

tensity (Figure 4c). These findings correspond to the low photovoltaic performance of the corresponding device due to low *Jsc* caused by low absorptivity of the oligomer which is caused by unfavorable orientation of the donor molecules. After 30 s of SVA, the absorption intensity for the oligomer strongly increased indicating that the SVA treatment led to higher order of the donor material.[5,6] While changes in the absorption spectrum are similar for the two molecules **1** and **2**, the EQE spectra of **2** showed higher EQE values in the absorption range of the oligomer (500-800 nm) indicating that the photocurrent generation inside the donor phase is improved compared to devices using oligomer **1**. In the following, we studied the question, in how far the movement of the branching point from C2 of the side chain of **1** to C4 of **2** may lead to an increased photocurrent and, more importantly, to very high fill factors of up to 75%. Thermal stability of optimized solar cells using oligomer **2** with a blend ratio of 1:2 and SVA time of 30 sec was studied under thermal stress of two different temperatures, i.e. 120°C and 140°C. Complete devices were exposed to the annealing step for 15 min. We found that the solar cell performance of initially 8.16 % decreased rapidly to 4.02 % and 2.33 % after thermal stress of 120°C and 140°C, respectively, as shown in Figures S1 and Table S1 (Supporting information, SI). Importantly, the device structure itself including corresponding interfacial layers of PEDOT:PSS and ZnO is thermally stable under such temperatures as demonstrated recently.[18] This indicates that the thermal stability of the photoactive layer at elevated temperature is limited demanding for further improvements via chemical engineering of the donor structure or combination with non-fullerene acceptors.

5. Electronic and morphological investigations of 2:$PC_{71}BM$ blends during solvent vapor annealing (SVA)

One of the reasons for an improvement in fill factor is a better balance in charge transport inside the blend; therefore, we first processed field-effect transistors with both oligomeric do-

View Article Online
DOI: 10.1039/C7QO00222J

nors **1** and **2** to determine the hole mobility as a function of SVA annealing time. As it can be seen in Table **S2**, the movement of the branching point from C2 of the side chain of **1** to C4 of **2** reduces the mobility by about one order of magnitude from ~5 x 10^{-4} $cm^2V^{-1}s^{-1}$ for **1** to ~6 x 10^{-5} $cm^2V^{-1}s^{-1}$ for **2** in the case of as-cast layers. After SVA of 30 s, we observe an increase in mobility by about one order of magnitude for both molecules (**1**: ~1 x 10^{-3} $cm^2V^{-1}s^{-1}$; **2**: ~1 x 10^{-4}), but the mobility of **2** is still smaller than this of **1**. These analyses showed that changing the branching point impacts the electronic properties of the oligomer thin films by reducing hole mobility in the case of **2**. This is in contrast to recent studies, as there an improvement in hole mobility was found.[5–8] Due to the fact that the electron mobility in $PC_{71}BM$-based polymer blends is usually in the range of 10^{-4} cm^2/Vs to 10^{-3} cm^2/Vs as a function of the donor,[19,20] we can conclude that the hole transport properties of both co-oligomers **1** and **2** can lead to sufficiently balanced hole and electron transport inside the bulk heterojunction. As the latter depends strongly on the nanoscale morphology of the donor and fullerene phases inside the blend, a detailed morphological study of the **2**:$PC_{71}BM$ blend is essential for better understanding of the FF increase in solar cells based on oligomer **2**. To establish a deeper understanding of the impact of the branching position on the donor crystallinity alone and in the presence of $PC_{71}BM$, two-dimensional grazing incidence X-ray diffraction (2D-GIXRD) measurements were performed on pure **2** layers as well as on **2**:$PC_{71}BM$-blends before and after 30 s SVA (Figure 5a). For these pure layers of oligomer **2**, the patterns showed clear out-of-plane diffraction peaks for (100), (200), and (300), corresponding to a lamellar stacking of donor molecules and an in-plane π-π stacking diffraction peak. This implies that molecules **2** preferentially adopt an edge-on orientation. Profiles along the (100) peak before and after the 30 s SVA treatment (Figure 5b) showed the enhancement of the (100) peak intensity implying an increased crystallinity of **2** upon SVA. By adding $PC_{71}BM$, a broad non-oriented halo corresponding to the fullerene component appears in the patterns. Nevertheless, by the observation of the same characteristics assigned to **2**, blending with $PC_{71}BM$ does not drama-

View Article Online
DOI: 10.1039/C7QO00222J

tically change the orientation or spacing of the lamellae. Similar to and as observed previously for oligomer **1**, the crystallinity of donor molecules blended with fullerenes increased by applying a short SVA time.[8]

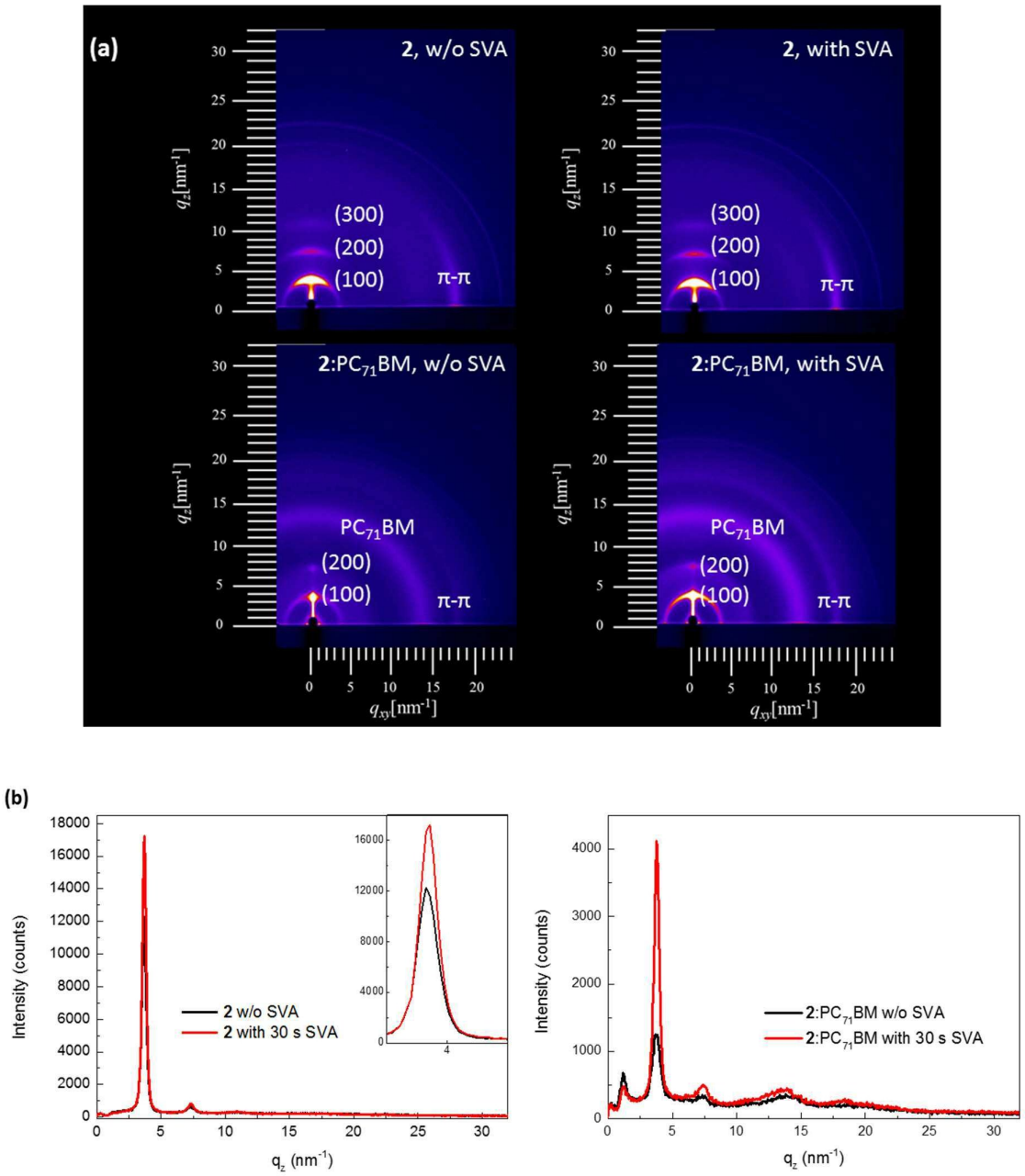

Figure 5: a) Two dimensional diffraction patterns of pure oligomer **2** layers before (black) and after a 30 s SVA treatment (red). **b)** Profiles along the (100) peak before (black) and after the 30 s SVA treatment (red) of **2**:$PC_{71}BM$ blend layers.

View Article Online
DOI: 10.1039/C7QO00222J

Compared to pure layers of **1** (Figure S3), a slight shift of the (100) peak to smaller scattering vectors (low q_z) indicates a thicker lamellar structure for **2** in pure layers. However, this difference tends to disappear for blend layers with similar lamellar structures after a 30 s SVA (Figure S4). The π-π stacking distance between the backbones is not impacted by the movement of the branching point of the 2-hexyldecyl chain in **1** to the C4-position resulting in a 4-hexyldecyl side chain in **2** whether in pure or in blend layers.

In order to gain deeper insight into the nanoscale morphology of the photoactive layer, spectroscopic imaging using a combination of scanning transmission electron microscopy and low-energy-loss spectroscopic imaging (STEM-SI) was applied to visualize the time evolution of nanoscale morphological changes of **2**:$PC_{71}BM$ blends as a function of SVA time.[21] Indeed STEM-SI has been proven to be a reliable technique in order to distinguish between donor and acceptor phases with the high spatial resolution of the electron microscope.[22,23] The analyzed blend layers were fabricated according to the parameters used for the fabrication of the solar cells (Table 2) and transferred to an electron microscopy grid. Thereby, it was possible to visualize spatial differences and distinguish D- and A-rich domains in the bulk heterojunction by mapping the peaks of the spatially resolved volume plasmons. Red regions were assigned to $PC_{71}BM$ and the green ones to oligomer **2**-enriched phases.

The plasmon-peak map for the as-cast blend is depicted in Figure 6a. The image indicates strongly mixed phases of oligomer **2** and $PC_{71}BM$-enriched phases lacking phase separation on a scale larger than a few nanometers. The plasmon-peak map indicates stronger accumulation of a $PC_{71}BM$-rich phase throughout the entire blend compared to discontinuous donor phases. These findings correspond to the low photovoltaic performance of the corresponding device with low FF caused by high bi-molecular recombination rates. The corresponding map for the blend layer treated by 10 s SVA shows a slowly evolving and fine phase separation of the two materials and apparently donor-rich domains start to grow and to form a network (Figure 6b). This relatively small change in morphology already caused a substantial improve-

View Article Online
DOI: 10.1039/C7QO00222J

ment of the parameters, i.e., a strong increase of J_{SC} from 3.44 to 12.59 mA cm^{-2} and FF from 29 to 57% resulting in an improvement in PCE from 0.77 to 5.66% (Table 2). The increase of the SVA time to 30 seconds results in a transformation of the blend into a nanostructured layer of well-defined, enlarged bicontinuous donor- and acceptor-rich phases where **2**-enriched domains are embedded in highly-connected $PC_{71}BM$-enriched domains (Figure 6c). As a consequence, the photovoltaic parameters were further improved, in particular to a considerable J_{SC} of 13.62 mA cm^{-2}, FF of 75%, and PCE of 8.16%. Longer exposition times to chloroform vapor resulted in further enhanced phase separation as illustrated in Figure 6d. After 60 s of SVA, the plasmon-peak map of the blend revealed a coarsening of the blend layer morphology caused by further growth of the donor and acceptor phases and merging of donor-rich domains. Increasing domain sizes of both components signifies decreased interfacial area in the BHJ and is reflected by a decline of the photovoltaic parameters of the corresponding solar cells. In particular, J_{SC} decreased to 10.52 mA cm^{-2} resulting in an efficiency of 6.06%. Since longer exposure times to chloroform vapor would clearly further enhance the phase separation and concomitant domain growth, a progressive decrease of the photovoltaic performance was expected and corresponding experiments were not any more undertaken.

In order to get an estimation of the nanophase dimensions at various SVA times, power spectral densities (PSD) were calculated for the laterally resolved images in Figure 6a-d (Figure S5). PSDs are rotationally averaged profiles of the power spectrum and thereby offer determination of predominant spatial features in the frequency domain. For the as-cast layer no peak could be identified. For 10 s SVA still no distinct peak can be observed, but a shoulder between 0.05-0.08 1/nm which corresponds to domain sizes of 10-20 nm. For 30 s SVA a broader peak at 0.02 1/nm which corresponds to 50 nm domain size and at 60 s SVA a peak at 0.012 1/nm corresponding to 83 nm are clearly visible.

View Article Online
DOI: 10.1039/C7QO00222J

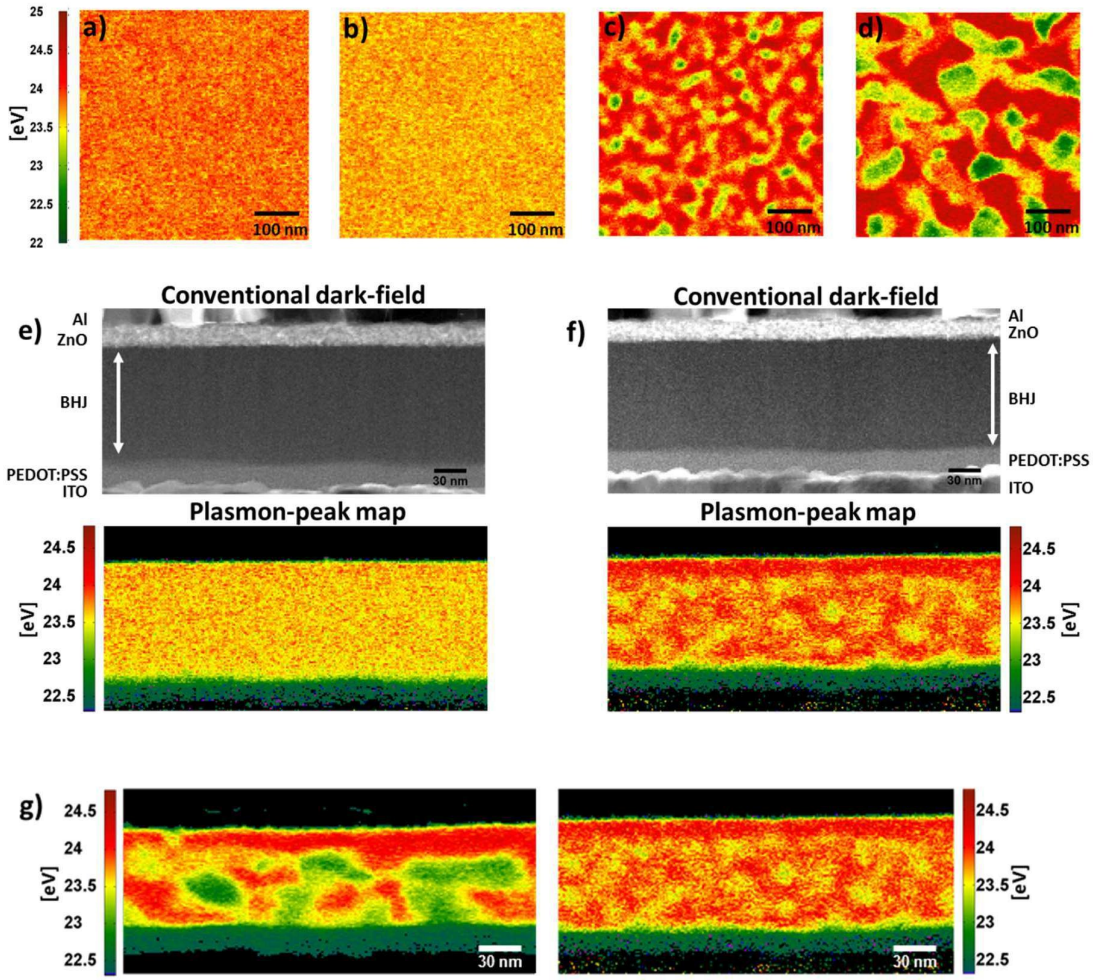

Figure 6: Plasmon-peak maps for the oligomer **2**:$PC_{71}BM$ blend: **a)** as-cast; **b)** after 10 s SVA; **c)** after 30 s SVA; **d)** after 60 s SVA**.** Dark-field image and plasmon-peak map of the corresponding device cross-sections **e)** as-cast and **f)** after 30 s SVA**. g)** Plasmon-peak map for the oligomer **1**/$PC_{71}BM$ blend (left) after 30 s of SVA in comparison to blend of **2**/$PC_{71}BM$ blend (right) after 30 s of SVA.[8]

STEM-SI analyses were performed on device cross-sections elucidating the vertical distribution of donor and acceptor. Conventional dark-field and plasmon-peak maps were taken for the two extremes, as-cast devices with lowest and devices after 30 s of SVA with best performances. In accordance with the lateral maps, the vertical plasmon-peak map for the as-cast device showed intimately mixed donor and acceptor phases (Figure 6e). For the best performing devices, the blend layer mostly resembles a homogenously phase-separated bulk-heterojunction concurring with the lateral plasmon-peak map. However, on top of the photoactive layer we note an accumulation of acceptor domains towards the ZnO-interface, whereas at the

View Article Online
DOI: 10.1039/C7QO00222J

bottom a small oligomer **2**-rich layer at the PEDOT:PSS-interface is identified (Figure 6f). This composition gradient of the photoactive layer obviously guarantees efficient charge carrier generation in the middle part of the blend combined with optimized charge extraction at the interfaces towards the respective electrodes. These time-resolved analyses of SVA treated **2**:$PC_{71}BM$-blends finally allow identification of the major impact of the alteration in the branching point from C2 of the side chain of **1** to C4 of **2**. Indeed, compared to the time evolution of **1**:$PC_{71}BM$ blends under SVA, the modification of donor **2** allows for slowing down donor and acceptor diffusion inside the blend. While the blend morphology before SVA can be considered as identical for both molecules, plasmon-peak maps already after 10 s show different morphologies. Indeed, phase separation in the case of **2**:$PC_{71}BM$ blends is less pronounced than in the case of **1**:$PC_{71}BM$ blends. After 30 s SVA, which corresponds to optimal processing time for both molecules, smaller donor and acceptor-enriched domain sizes are formed in the case of oligomer **2**-based blends compared to those using **1**. Furthermore, the cross section reveals a thinner $PC_{71}BM$-enriched top layer at the ZnO-interface as well as a **2**-enriched layer at the PEDOT: PSS-interface. The vertical cross-section of the **2**:$PC_{71}BM$ blend rather resembles a nanostructured bulk heterojunction with external enriched layers than a nanostructured bilayer as observed before for **1**. This may be one of the reasons of the drop in V_{OC} observed for **2**-based devices. The quasi optimal morphology of **2**-based BHJSCs is responsible for the very high FF in combination with the improved J_{SC} compared to **1** as shown in Table 2. It is important to highlight that the **2**:$PC_{71}BM$ blend treated for only 10 seconds consists of extremely small enriched domains (below 5 nm and thus towards the detection limit given by the STEM-SI settings) but still produce 5.66 % efficient solar cells with FF of 59%. By the fact that blends using oligomer **1** showed lower performance although the size of the donor and acceptor domains, respectively, is larger and thus more suitable to produce efficient photocurrent generation, we deduce that oligomer **2** is able to form donor domains of increased purity already at small sizes. This interpretation is supported not only by the higher FF,

View Article Online
DOI: 10.1039/C7QO00222J

but also by the observation that solubility of **2** in a common solvent such as chloroform is smaller than for **1** indicating that intermolecular interaction is increased and thus the tendency to form pure domains.

6. Conclusion

In conclusion, subtle structural modification, i.e., shifting the branching point in the side chains away from the conjugated backbone, in a well-studied dithienopyrrole-based A-D-A oligothiophene has been applied to improve power conversion efficiency of SVA-treated bulk-heterojunction solar cells. While optoelectronic properties were found not to be influenced by the chemical modification of the alkyl substitution pattern, efficiency of the solution-processed solar cells could be increased to 8.2%. Time-dependent evolution studies of the micro- and nanoscale morphology of blends during solvent vapor annealing reveal that domain size and domain purity could be improved inside the blend consisting of oligomer **2** and $PC_{71}BM$. The latter is addressed to slowing down donor and acceptor diffusion during SVA through reduction in solubility and compatibility of the donor with the fullerene derivate.

7. Experimental Section

Instruments and measurements: ^{1}H NMR spectra were recorded in deuterated solvents as specified in the synthetic procedures on a Bruker AMX 400 at 400 MHz. $^{13}CNMR$ spectra were recorded on a Bruker AMX 400 at 100 MHz. Chemical shifts are denoted by a δ unit (ppm) and are referenced to corresponding residual solvent peaks of the utilized deuterated solvent. The splitting patterns are designated as follows: s (singlet), d (doublet), t (triplet), and m (multiplet). Mass spectra were recorded with a Varian Saturn 2000 GC-MS and with a MALDI-TOF MS Bruker Reflex 2 (matrix: trans-2-[3-(4-tert-butylphenyl)-2-methyl-2-propenylidene]-

View Article Online
DOI: 10.1039/C7QO00222J

malononitrile (DCTB). High resolution MALDI MS was measured on a Fourier Transform Ion Cyclotron Resonance (FT-ICR) mass spectrometer solariX from Bruker Daltonics equipped with a 7.0 T superconducting magnet and interfaced to an Apollo II Dual ESI/MALDI source. CI-MS measurements were recorded on a Finnigan MAT, SSQ-7000. Melting points of the intermediates were determined with a Büchi B-545 melting point apparatus and are not corrected. Melting points of target compounds were measured via differential scanning calorimetric measurements (DSC) on a Mettler Toledo DSC823e under argon atmosphere at a heating rate of 10 °C min. Thin-layer chromatography was carried out on Silica Gel 60 F254 aluminum plates (Merck). Solvents and reagents were purified and dried by usual methods prior to use and used under inert gas atmosphere. UV-vis spectra in DCM solution and thin film were taken on a Perkin-Elmer Lambda 19 spectrometer. Cyclic voltammetry experiments were performed with a computer-controlled Autolab PGSTAT30 potentiostat in a three-electrode single compartment cell (3 mL). The platinum working electrode consisted of a platinum wire sealed in a soft glass tube with a surface of A = 0.785 mm2, which was polished down to 0.25 μm with Buehler polishing paste prior to use to guarantee reproducible surfaces. The counter electrode consisted of a platinum wire and the reference electrode was an Ag/ AgCl reference electrode. All potentials were internally referenced to the ferrocene/ ferricenium couple. For the measurements, concentrations of 10^{-3} M of the electroactive species were used in freshly distilled and deaerated DCM (Lichrosolv, Merck) purified with an Braun MB-SPS-800 and 0.1 M $(n\text{-}Bu)_4NPF_6$ (Fluka; recrystallized twice from ethanol).

Device fabrication and photovoltaic characterization: Photovoltaic devices were made by spin-coating PEDOT:PSS (Clevios P, VP Al4083) onto pre-cleaned, patterned indium tin oxide (ITO) substrates (15 Ω/cm^2) (Kintec). The photoactive layer was deposited by spin-coating donor **2** and $PC_{71}BM$ ([6,6]-phenyl-C_{71}-butyric acid methyl ester, 99% purity purchased from Nano-C) from chloroform solutions (total concentration = 24 mg/mL) without additives leading to layer thicknesses of ~90-100 nm. The devices for oligomer **2** were fabricated by

View Article Online
DOI: 10.1039/C7QO00222J

spin-coating at room temperature. The counter electrode aluminum (100 nm) was deposited by vacuum evaporation at 2 x 10^{-6} torr. The active areas of the cells were 0.27 cm^2. Film thicknesses were measured using a Dektak profilometer.

The current density-voltage (J-V) characteristics of the devices were measured using a Keithley 238 Source Measure Unit inside the glovebox using Lumtec substrates. Solar cell performance was measured by using a Newport class AAA 1.5 Global solar simulator (Oriel Sol3 ATM model n° 94043A) with an irradiation intensity of 100 mW cm^{-2}. The light intensity was determined with a Si reference cell (Newport Company, Oriel n°94043A) calibrated by National Renewable Energy Laboratory (NREL). Shadow masks were used to well define the illuminated area to 0.27 × 1.0 cm^2. Comparison of masked and unmasked solar cells gave consistent results with photocurrent increase by less 3 % for unmasked devices. We present performance of the best devices, while average PCEs were obtained with standard deviation analysis calculated using nine devices. External quantum efficiency measurements were performed in air using a homemade setup consisting of a Keithley 238 Source Measure Unit and Newport monochromator. Light intensity was measured with a calibrated Si-diode from Newport Company.

Transmission Electron Microscopy: STEM-SI measurements were performed at 120 kV using a Titan 60-300 microscope (FEI) and an Enfinium spectrometer (Gatan). Planar specimens were prepared by floating the photoactive layer off the substrate through dissolving of the PEDOT:PSS layer followed by capturing with an electron microscopy grid covered with a holey carbon film (QUANTIFOIL®). Cross-sections were prepared on solar cell devices with a Helios Nanolab 650 (FEI). Scanning step sizes for STEM-SI imaging were set to 3 nm for planar analyses, and to 1.5 nm for cross-sectional analyses. Spatially resolved spectroscopic data sets were processed and fitted using HyperSpy as explained previously.[21] Power spectral densities were calculated using the software package SPIDER (System for Processing Image Data from Electron microscopy and Related fields, Wadsworth Center).

View Article Online
DOI: 10.1039/C7QO00222J

Materials: The following starting materials were purchased and used without further purification: malononitrile (Aldrich), n-butyl lithium (ACROS), trimethyltin chloride (Aldrich), (±)-BINAP (Aldrich), tris(dibenzylideneacetone)dipalladium(0) (Aldrich), benzyl bromide (Merck), 1,4-butanediole (Fluka), sodium hydride (Merck), chromium(VI) oxide, triethyl silane (Merck), triphenylphosphine (Merck), imidazole (Aldrich), sodium azide (Aldrich), lithiumaluminum hydride (Merck), 1,3-cyclohexandione (Aldrich), iron(III) tosylate (Merck), 2-isopropoxy-4,4,5,5-tetramethyl-1,3,2-dioxaborolane (Merck), phosphoroxy chloride (Merck), tetrakis(triphenylphosphine)palladium(0), 3,3'-dibromo-2,2'-bithiophene, and 2-[(5'-bromo-3, 4'-dihexyl[2,2'-bithien-5-yl])methane-1-yl-1-ylidine]malononitrile were synthesized according to literature.[5,22]

Synthesis: *4-(Benzyloxy)butane-1-ol (**4**).* 1,4-Butanediole (**3**) (44.8 mL, 0.50 mol, 2 eq) was dissolved in 200 mL dry THF and was cooled to 0°C. Sodium hydride (10.1 g, 0.25 mol, 60%, 1 eq) was added to the solution in batches over 30 min. Then, the ice bath was removed and the reaction was stirred for 14 h until the formation of hydrogen stopped. After cooling to 0°C again, benzyl bromide (30.0 mL, 0.25 mol, 1 eq) dissolved in 20 mL dry THF was added dropwise to the reaction mixture. The solution refluxed over night before it was quenched with cold water (150 mL). The organic phase was extracted with diethyl ether (3 x 200 mL) and the combined organic layers were dried over anhydrous $NaSO_4$ before the solvent was removed under reduced pressure. Alcohol **4** was distilled at pressure of 1.6 x 10^{-1} mbar at 129°C as a colorless liquid (42.0 g, 0.23 mol, 93.3%). ^{1}H-NMR (400 MHz, CD_2Cl_2): δ [ppm] = 7.40-7.24 (m, 5H, Ph), 4.50 (s, 2H, Ph-CH_2), 3.57 (t, J = 6.2 Hz, 2H, Bn-O-CH_2), 3.49 (t, J = 6.1 Hz, 2H, HO-CH_2-), 1.74–1.58 (m, 4H, CH_2). ^{13}C-NMR (100 MHz, $CDCl_3$): δ [ppm] = 138.16, 128.41, 127.71, 127.63, 73.03, 70.32, 62.70, 30.14, 26.64. The analytical data are in accordance with the literature data.[15]

*Ethyl-4-(benzyloxy)butanoate (**5**).* Chromium(VI)oxide (26.7 g, 267 mmol, 4.4 eq) was added to 23 mL of concentrated sulfuric acid and the suspension was diluted to 100 mL with de-

View Article Online
DOI: 10.1039/C7QO00222J

ionized water. The suspension was added dropwise to solution of **4** (11.0 g, 61.0 mmol, 1 eq) in 200 mL acetone at 0°C. After stirring for 2 h at rt, the resulting mixture was vacuum filtered through a silica column, eluted with acetone. The solvent was evaporated and the residue was extracted with EA (3 x 200 mL). The combined organic layers were washed with brine (3 x 150 mL) and dried over anhydrous $MgSO_4$. After the solvent was removed, the crude oil was dissolved in 100 mL ethanol and 2 mL of concentrated sulfuric acid were added before refluxing for 72 h. The reaction mixture was extracted with ethyl acetate (3 x 150 mL) and the organic layers were combined. The organic phase was subsequently washed with a $NaHCO_3$-solution (200 mL), deionized water (200 mL), and brine (200 mL) before it was dried over anhydrous $MgSO_4$. The solvent was removed with the rotary evaporator before product **5** was distilled at 120°C and 1.8 x 10^{-1} mbar (11.3 g, 50.7 mmol, 83.0%). ^{1}H-NMR (400 MHz, $CDCl_3$): δ [ppm] = 7.34–7.20 (m, 5H), 4.47 (s, 2H), 4.10 (q, J = 7.1 Hz, 2H), 3.48 (t, J = 6.2 Hz, 2H), 2.41 (t, J = 7.4 Hz, 2H), 1.97–1.89 (m, 2H), 1.22 (t, J = 7.1 Hz, 3H). ^{13}C NMR (100 MHz, $CDCl_3$): δ [ppm] = 173.16, 138.20, 128.05, 127.29, 127.24, 72.50, 68.85, 59.95, 30.78, 24.82, 13.92. The analytical data are in accordance with the literature data.[15]

*7-(3-(Benzyloxy)propy)tridecan-7-ol (**6**).* Hexylmagnesium bromide (48.5 g, 256 mmol, 2.5 eq.) was synthesized by carefully adding 1-bromohexane (36.7 mL, 256.1 mmol, 2.5 eq) to magnesium flakes (6.23 g, 256 mmol, 2.5 eq) submerged in 65 mL dry diethyl ether and refluxed for 4 h under argon. The reaction mixture was cooled to 0°C before **5** (22.8 g, 102 mmol, 1.0 eq) was added dropwise. After stirring for 10 min at rt, the reaction mixture was refluxed for 18 h. Then, the mixture was cooled to 0°C and water (50 mL) and diethyl ether (50 mL) were added carefully. The solution was then neutralized with 2M hydrochloric acid. The layers were separated and the aqueous phase was extracted with diethyl ether (3 x 100 mL). The combined organic layers were washed with brine (3 x 100 mL) before drying over anhydrous $MgSO_4$. The solvent was removed under reduced pressure and the resulting crude product was purified via flash chromatography (SiO_2, dichloromethane:ethyl acetate 97:3).

View Article Online
DOI: 10.1039/C7QO00222J

The desired alcohol **6** could be isolated as a colorless liquid (20.3 g, 58.1 mmol, 56.7%). ^{1}H-NMR (400 MHz, $CDCl_3$): δ [ppm] = 7.42-7.14 (m, 5H), 4.49 (s, 2H), 3.47 (t, J = 6.3 Hz, 2H), 1.71-1.61 (m, 2H), 1.43-1.21 (m, 22H), 0.90 (t, J = 6.7 Hz, 6H). ^{13}C-NMR (100 MHz, $CDCl_3$): δ [ppm] = 138.23, 128.13, 127.39, 127.31, 73.70, 72.65, 70.79, 39.02, 35.80, 31.76, 29.88, 23.71, 23.37, 22.55, 13.95. MS (CI): *m/z* [M^+-H] = 346, [M^+-Ph-CH_2-O] = 242.

{[(4-Hexyldec-3-en-1-yl)oxy]methyl}benzene (7). Tertiary alcohol **6** (20.3 g, 58.1 mmol, 1.0 eq) was dissolved in 100 mL dry dichloromethane, to which triethylsilane (11.1 mL, 69.7 mmol, 1.2 eq) and trifluoroacetic acid (22.4 mL, 291 mmol, 5.0 eq) were added. After stirring for 16h at rt, the reaction was quenched by adding Na_2CO_3 until no gas was formed anymore. The suspension was loaded onto a short silica gel column, eluted with dichloromethane. Then, the solvent was removed under reduced pressure and the crude oil was purified via flash chromatography (SiO_2, 5:2 petrol ether:dichloromethane) affording the desired product **7** as a colorless liquid (10.0 g, 30.3 mmol, 52.1%). ^{1}H-NMR (400 MHz, CD_2Cl_2): δ [ppm] = 7.37-7.25 (m, 5H, Ph), 4.52 (s, 2H, Ph-CH_2), 3.49 (t, J = 6.2 Hz, 2H, BnO-CH_2), 1.72-1.64 (m, 2H, BnO-CH_2-CH_2), 1.56-1.29 (m, 23H, CH_2), 0.93 (t, J = 6.8 Hz, 6H, -CH_3). ^{13}C-NMR (100 MHz, $CDCl_3$): δ [ppm] = 141.85, 138.33, 128.23, 127.50, 127.31, 75.73, 72.75, 70.89, 39.11, 35.81, 31.85, 29.90, 23.72, 23.35, 22.57, 13.93. MS (CI): *m/z* [M^++2H] = 332, [M^+-Ph-CH_2-O] = 223.

*4-Hexyldecan-1-ol (**8**).* Molecule **7** (1.38 g, 4.17 mmol) was dissolved in 50 mL ethyl acetate, to which 10% Pd/C (125 mg) was carefully added. The suspension was purged slowly with hydrogen for 18 h at rt. Afterwards, the suspension was filtered through a flash silica column, eluted with ethyl acetate. The solvent was evaporated under reduced pressure and the resulting crude liquid was purified via flash chromatography (SiO_2, dichloromethane) to afford the desired alcohol **8** as a colorless liquid (0.96 g, 3.97 mmol, 95.1%). ^{1}H-NMR (400 MHz, $CDCl_3$): δ [ppm] = 3.16 (t, J = 7.1 Hz, 2H), 1.84-1.75 (m, 2H), 1.35-1.22 (m, 23H),

View Article Online
DOI: 10.1039/C7QO00222J

0.89 (t, J = 6.9 Hz, 6H). ^{13}C NMR (100 MHz, $CDCl_3$): δ [ppm] = 63.31, 37.38, 33.71, 32.07, 29.96, 29.94, 29.71, 26.76, 26.74, 22.82, 14.16. MS (CI): *m/z* [M^+-H] = 241, [M^+-OH] = 225.

*4-Hexyldecyl-1-iodide (**9**).* Alcohol **8** (962 mg, 3.97 mmol, 1.0 eq), imidazole (351 mg, 5.16 mmol, 1.3 eq), and triphenylphosphine (1.35 g, 5.16 mmol, 1.3 eq) were dissolved in 250 mL DCM at rt. The solution was cooled to 0°C and iodine (1.31 g, 5.16 mmol, 1.3 eq) was added slowly. The ice bath was removed and the reaction mixture stirred at rt for 18 h. The reaction was terminated by the addition of a saturated thiosulphate solution and the phases were separated. The aqueous phase was extracted with DCM (3 x 150 mL) before the combined organic layers were subsequently washed with deionized water (3 x 100 mL) and brine (3 x 100 mL). After removing the solvent under reduced pressure, the crude product was purified via flash chromatography (SiO_2, petrol ether). Target molecule **9** was obtained as a colorless liquid (1.35 g, 3.83 mmol, 96.5%). ^{1}H-NMR (400 MHz, $CDCl_3$): δ [ppm] = 3.58 (t, J = 6.8 Hz, 2H), 1.56-1.45 (m, 2H), 1.29-1.21 (m, 23H), 0.86 (t, J = 6.9 Hz, 6H). ^{13}C-NMR (100 MHz, $CDCl_3$): δ [ppm] = 37.32, 36.85, 36.25, 34.68, 33.83, 33.72, 32.12, 32.07, 31.06, 30.00, 29.90, 26.80, 26.75, 22.85, 19.96, 14.70, 14.26, 7.58. MS (EI): *m/z* [M^+] = 352.

*4-Hexyldecyl-1-azide (**10**).* Iodide **9** (7.57 g, 21.5 mmol, 1.0 eq) was dissolved in dry DMF in an argon atmosphere and sodium azide (6.70 g, 103 mmol, 4.8 eq) was added in batches. The suspension stirred at 85°C for 4 h. DMF was removed by vacuum distillation and the raw product was extracted with petrol ether (3 x 200 mL). The combined organic layers were washed with brine (3 x 100 mL) and dried over anhydrous Na_2SO_4. The solvent was removed under reduced pressure to give the pure azide **10** as a colorless liquid (5.10 g, 19.1 mmol, 88.7%). ^{1}H-NMR (400 MHz, $CDCl_3$): δ [ppm] = 3.23 (t, J = 7.0 Hz, 2H), 1.63-1.52 (m, 2H), 1.36-1.19 (m, 23H), 0.89 (t, J = 6.9 Hz, 6H). ^{13}C NMR (100 MHz, $CDCl_3$) δ [ppm] = 52.02, 37.24, 33.65, 32.07, 30.71, 29.91, 26.72, 26.20, 22.84, 14.19. MS (CI): *m/z* [M^+-N_2] = 239.

*4-Hexyldecyl-1-amine (**11**).* Lithium aluminum hydride (1.09 g, 28.7 mmol, 1.5 eq) was added to a solution of azide **10** (5.12 g, 19.1 mmol, 1.0 eq) in 350 mL dry diethyl ether. After

View Article Online
DOI: 10.1039/C7QO00222J

refluxing for 1 h, moist diethyl ether (50 mL) was added, followed by the addition of a 15% aqueous sodium hydroxide solution (50 mL). The layers were separated before the organic phase was washed with brine (1 x 50 mL) and deionized water (3 x 150 mL). After drying over anhydrous magnesium sulphate and evaporation of the solvent, 4-hexyldecan-1-amine **11** was obtained as a colorless liquid (3.98 g, 16.5 mmol, 86.1%). ^{1}H-NMR (400 MHz, $CDCl_3$): δ [ppm] = 2.61-2.57 (t, J = 7.0 Hz, 2H), 1.34 (m, 2H), 1.23-1.14 (m, 23H), 1.06 (s, 2H), 0.82 (t, J = 6.9 Hz, 6H). ^{13}C-NMR (100 MHz, $CDCl_3$): δ [ppm] = 42.70, 37.37, 37.25, 36.18, 33.76, 33.70, 32.03, 30.88, 30.76, 29.92, 29.89, 26.72, 22.79, 19.89, 14.62, 14.19. HR-MS (ESI): *m/z* [M^++H] = 242.28428 (calc. for $C_{16}H_{36}N$: 242.28478).

*N-(4-Hexyldecyl)dithieno[3,2-b:2',3'-d]pyrrole (**13**).* 3,3'-Dibromo-2,2'-bithiophene **12** (2.60 g, 8.02 mmol, 1.0 eq), sodium-*tert*-butoxide (1.85 g, 19.25 mmol, 2.4 eq), BINAP (0.52 g, 0.80 mmol, 0.1 eq), and $Pd_2dba_3{\cdot}CHCl_3$ (208 mg, 0.24 mmol, 0.03 eq) were mixed in 20 mL dry toluene and the suspension was purged with argon for 15 min. 4-hexyldecan-1-amine (2.00 g, 8.26 mmol, 1.03 eq) was added and the mixture stirred at 110°C for 18 h. After cooling, water was added and the organic layer was separated. The aqueous phase was extracted with diethyl ether (3 x 150 mL). The combined organic layers were dried over anhydrous Na_2SO_4 and the solvent was removed under reduced pressure. Finally the crude product was purified by column chromatography (SiO_2, 5:3 petroleum ether:dichloromethane) to afford product **13** as a colorless oil (3.04 g, 7.53 mmol, 93.8%). ^{1}H-NMR (400 MHz, CD_2Cl_2): δ [ppm] = 7.17 (d, J = 5.3 Hz, 2H, α-H), 7.05 (d, J = 5.3 Hz, 2H, β-H), 4.20 (t, J = 7.2 Hz, 2H, N-CH_2), 1.90 (qui, J = 7.3 Hz, 2H, N-CH_2-CH_2), 1.38-1.25 (m, 23H, CH_2), 0.97 (t, J = 7.0 Hz, 6H, CH_3). ^{13}C-NMR (100 MHz, $CDCl_3$): δ [ppm] = 144.99, 122.77, 114.73, 111.02, 47.89, 37.08, 33.55, 32.02, 30.78, 29.85, 27.39, 26.65, 22.84, 14.27. MS (CI): *m/z* [M^++H] = 404.

*2,5'-Bis(trimethylstannyl)-N-(4-hexyldecyl)dithieno[3,2-b:2',3'-d]pyrrole (**14**).* Dithienopyrrole **13** (1.08 g, 2.66 mmol, 1.0 eq) was dissolved in 15 mL dry THF in an argon atmosphere and the solution was cooled to -78 °C. *N*-Butyl lithium (1.6 M, 3.99 mL, 6.39

View Article Online
DOI: 10.1039/C7QO00222J

mmol, 2.4 eq) was added dropwise and the solution stirred 1h at -78 °C, then warmed up to 0°C and stirred again for 1 h. The reaction mixture was cooled to -78 °C and trimethylstannyl chloride (1.33 g, 6.66 mmol, 2.5 eq) dissolved in 5 mL dry THF was added swiftly. The mixture stirred for 2.5 h at -78 °C before the reaction was terminated by adding petroleum ether (30 mL) and washing with deionized water (3 x 50 mL). The solvent was evaporated under reduced pressure and afforded distannyl **14** as a dark green liquid (1.94 g, 2.65 mmol, 100%). The product was used without further purification. ^{1}H-NMR (400 MHz, THF-*d2*): δ [ppm] = 7.11 (s, 2H, β-H), 4.23 (t, J = 7.1 Hz, 2H, N-CH_2), 1.91-1.81 (m, 2H, N-CH_2-CH_2), 1.34-1.19 (m, 23H, CH_2), 0.88 (t, J = 6.9 Hz, 6H, CH_3), 0.38 (s, 18H, Sn-CH_3).

*2,2'-[(N-(4-Hexyldecyl)dithieno[3,2-b:2',3'-d]pyrrole-2,6-diyl)bis((3,4'-dihexyl-2,2'-bithien-5,5'-diyl)bis(methane-1-yl-1-ylidine)]dimalononitrile (**2**).* Distannyl **14** (300 mg, 0.41 mmol, 1.0 eq), dihexyl-bithiophene **15** (483 mg, 0.99 mmol, 2.4 eq), and tetrakis(triphenylphosphine)palladium(0) (19.0 mg, 26.5 µmol, 0.04 eq) were mixed in 20 mL dry DMF and the mixture was purged with argon for 20 min. The reaction mixture was stirred at 85°C for 18h. The reaction was cooled to rt before the product was precipitated with methanol. The suspension was filtered and the residue was washed with large amounts of methanol. The solid was dissolved in dichloromethane and the solution was washed with deionized water (3 x 150 mL). After drying over anhydrous Na_2SO_4, the solvent was evaporated under reduced pressure and the crude product was purified via flash chromatography (SiO_2, 2:1 dichloromethane:petroleum ether). The desired oligomer **2** could be isolated as dark purple solid (419 mg, 0.34 mmol, 83.4%). Mp: 174-178 °C. ^{1}H-NMR (400 MHz, $CDCl_3$): δ [ppm] = 7.67 (s, 2H, DCV-H), 7.50 (s, 2H, DCV-Th-β-H), 7.22 (s, 2H, DTP-Th-β-H), 7.09 (s, 2H, DTP-H), 4.21 (t, J = 6.9 Hz, 2H, N-CH_2), 2.85 (m, 8H, Th-CH_2), 1.95-1.84 (m, 2H, N-CH_2-CH_2), 1.77-1.65 (m, 8H, Th-CH_2-CH_2), 1.49-1.16 (m, 47H,-CH-CH_2), 0.91 (m, 12H; Th-alkyl-CH_3), 0.83 (t, J = 6.8 Hz, 6H, DTP-alkyl-CH_3). ^{13}C-NMR (100 MHz, $CDCl_3$): δ [ppm] = 149.93, 144.94, 144.19, 142.13, 140.60, 140.42 136.04, 133.21, 132.02, 131.71, 131.64,

View Article Online
DOI: 10.1039/C7QO00222J

115.88, 114.63, 113.73, 109.95, 75.54, 53.57, 48.05, 37.13, 33.57, 32.02, 31.80, 31.71, 30.85, 30.71, 30.08, 29.86, 29.68, 29.49, 29.44, 29.29, 27.40, 26.68, 22.79, 22.73, 14.22. HR-MS (MALDI-TOF): *m/z* [M^+] = 1219.57431 (calc. for $C_{72}H_{93}N_5S_6$: 1219.57498); δm/m = 0.27 ppm.

Supporting Information

Supporting Information is available from RSC.

Acknowledgements

We acknowledge financial support by the European Commission under the Project "SUNFLOWER" (FP7-ICT-2011-7, Grant number: 287594) and S.B. via the ERC Starting Grant Colouratoms (335078).

References

[1] A. Mishra, P. Bäuerle, *Angew. Chem. Int. Ed.* **2012**, *51*, 2020–2067.
[2] S.-H. Liao, H.-J. Jhuo, P.-N. Yeh, Y.-S. Cheng, Y.-L. Li, Y.-H. Lee, S. Sharma, S.-A. Chen, *Sci. Rep.* **2014**, *4*, 6813.
[3] J. De Chen, C. Cui, Y. Q. Li, L. Zhou, Q. D. Ou, C. Li, Y. Li, J. X. Tang, *Adv. Mater.* **2015**, *27*, 1035–1041.
[4] B. Kan, M. Li, Q. Zhang, F. Liu, X. Wan, Y. Wang, W. Ni, G. Long, X. Yang, H. Feng, Y. Zuo, M. Zhang, F. Huang, Y. Cao, T. P. Russell, Y. Chen, *J. Am. Chem. Soc.* **2015**, *137*, 3886–3893.
[5] C. D. Wessendorf, G. L. Schulz, A. Mishra, P. Kar, I. Ata, M. Weidelener, M. Urdanpilleta, J. Hanisch, E. Mena-Osteritz, M. Lindén, E. Ahlswede, P. Bäuerle, *Adv. Energy Mater.* **2014**, *4*, 1400266–1400276.
[6] C. D. Wessendorf, A. Perez-Rodriguez, J. Hanisch, A. P. Arndt, I. Ata, G. L. Schulz, A. Quintilla, P. Bäuerle, U. Lemmer, P. Wochner, E. Ahlswede, E. Barrena, *J. Mater. Chem. A* **2016**, *4*, 2571–2580.
[7] J. Min, X. Jiao, I. Ata, A. Osvet, T. Ameri, P. Bäuerle, H. Ade, C. J. Brabec, *Adv. Energy Mater.* **2016**, *6*, 1502579–1502588.
[8] S. Ben Dkhil, M. Pfannmöller, I. Ata, D. Duché, M. Gaceur, T. Koganezawa, N. Yoshimoto, J.-J. Simon, L. Escoubas, C. Videlot-Ackermann, L. Margeat, S. Bals, P. Bäuerle, J. Ackermann, *J. Mater. Chem. A* **2017**, *5*, 1005–1013.
[9] T. Lei, J. Y. Wang, J. Pei, *Chem. Mater.* **2014**, *26*, 594–603.
[10] Y. J. Kim, K. H. Park, J.-J. Ha, D. S. Chung, Y.-H. Kim, C. E. Park, *Phys. Chem. Chem. Phys.* **2014**, *16*, 19874–19883.
[11] T. Lei, J. H. Dou, J. Pei, *Adv. Mater.* **2012**, *24*, 6457–6461.
[12] J. P. Sun, A. D. Hendsbee, A. J. Dobson, G. C. Welch, I. G. Hill, *Org. Electron. physics, Mater. Appl.* **2016**, *35*, 151–157.
[13] T. Lei, X. Xia, J. Y. Wang, C. J. Liu, J. Pei, *J. Am. Chem. Soc.* **2014**, *136*, 2135–2141.
[14] M. Weidelener, C. D. Wessendorf, J. Hanisch, E. Ahlswede, G. Schulz, E. Mena-Osteritz, M. Lindén, A. Mishra, P. Bäuerle, *Chem. Commun.* **2013**, *49*, 10865–10867.
[15] X. Hu, M. Shi, L. Zuo, Y. Nan, Y. Liu, L. Fu, H. Chen, *Polymer* **2011**, *52*, 2559–2564.
[16] J. Pei, T. Lei, J. H. Dou, *Compound with Branching Alkyl Chains, Method for Preparing the Same, and*

View Article Online
DOI: 10.1039/C7QO00222J

Use Thereof in Photoelectric Device. US20140011973 A1, July 5th, **2013**.
[17] J. Cremer, E. Mena-Osteritz, N. G. Pschierer, K. Müllen, P. Bäuerle, *Org. Biomol. Chem.* **2005**, *3*, 985–95.
[18] S. Ben Dkhil, M. Pfannmöller, M. I. Saba, M. Gaceur, H. Heidari, C. Videlot-ackermann, O. Margeat, A. Guerrero, J. Bisquert, G. Garcia-belmonte, A. Mattoni, S. Bals, J. Ackermann, *Adv. Energy Mater.* **2017**, *7*, 1601486–1601497.
[19] S. Foster, F. Deledalle, A. Mitani, T. Kimura, K. Kim, T. Okachi, T. Kirchartz, J. Oguma, K. Miyake, J. R. Durrant, S. Doi, J. Nelson, *Adv. Energy Mater.* **2014**, *4*, 1400311.
[20] G. Juška, I. D. W. Samuel, B. Ebenhoch, S. A. J. Thomson, K. Genevic, *Org. Electron.* **2015**, *22*, 62–68.
[21] M. Pfannmöller, H. Heidari, L. Nanson, O. R. Lozman, M. Chrapa, T. Offermans, G. Nisato, S. Bals, *Nano Lett.* **2015**, *15*, 6634–6642.
[22] A. Guerrero, M. Pfannmöller, A. Kovalenko, T. S. Ripolles, H. Heidari, S. Bals, L. Kaufmann, J. Bisquert, G. Garcia-belmonte, *Org. Electron.* **2015**, *16*, 227–233.
[23] M. Pfannmöller, W. Kowalsky, R. R. Schröder, *Energy Environ. Sci.* **2013**, *6*, 2871.
[24] T. Phosphites, **1966**, 1186–1188.
[25] X. Zhang, T. T. Steckler, R. R. Dasari, S. Ohira, W. J. Potscavage, S. P. Tiwari, S. Coppée, S. Ellinger, S. Barlow, J.-L. Brédas, B. Kippelen, J. Reynolds, S. Marder, *J. Mater. Chem.* **2010**, *20*, 123–134.